The impact of ground-based glaciogenic seeding on a shallow stratiform cloud over the Sierra Madre in Wyoming: A multi-sensor study of the 3 March 2012 case

Binod Pokharel[*],[1], Bart Geerts, Xiaoqin Jing

Department of Atmospheric Science, University of Wyoming, Laramie, WY 82071, USA

ARTICLE INFO

ABSTRACT

A case study is presented of the impact of ground-based glaciogenic seeding on a shallow, lightly precipitating orographic storm with abundant supercooled cloud droplets, but few ice particles. The storm was observed on 3 March 2012 as part of the AgI (silver iodide) Seeding Cloud Impact Investigating (ASCII) experiment in Wyoming. The cloud base temperature was about −9 °C, and cloud tops were at about −16 °C. The high concentration of small droplets and low ice particle concentration lead to natural snow growth, mainly by vapor diffusion. The question addressed here is whether the injection of ice nucleating particles (AgI) enhanced snow growth and snowfall. The treated (seeded) period is compared with the preceding untreated (noseeded) period, and natural trends (observed in an adjacent control region) are removed. The main target site, located on a mountain pass at an elevation above cloud base, was impacted by AgI seeding, according to a trace chemistry analysis of freshly fallen snow.

Data from three radar systems were used: the Wyoming Cloud Radar, two Ka-band profiling Micro-Rain Radars, and a X-band scanning Doppler-on-Wheels (DOW) radar. Composite data from these radar systems and from gauges in the target area indicate an increase in low-level reflectivity and precipitation rate during seeding. This finding generally agrees with other published ASCII case studies. The increase in reflectivity during seeding in the target area appears to be due mainly to an increase in particle size (aggregation), not number concentration, as suggested by DOW differential reflectivity and by disdrometer and Cloud Particle Imager measurements on the ground.

1. Introduction

Cold-season snowfall over mountains is the main source of water in the western United States. Orographic clouds have been seeded to augment the snowpack over the western mountains for more than half a century. Orographic clouds often are suitable for glaciogenic seeding for several reasons: they are typically quite young and rich in supercooled liquid water (SLW) as air is lifted rapidly above the condensation level; and they are rather easy targets for ground-based seeding as they are often shallow and persistent. The efficacy of glaciogenic seeding remains poorly understood, notwithstanding many randomized experiments and field work focused on cloud microphysics (National Research Council, 2003; Garstang et al., 2005). This was the broader motivation for two recent field campaigns. The first one focused on

ground-based seeding: the AgI (silver iodide) Seeding Cloud Impact Investigation (ASCII) was conducted over the Sierra Madre in southern Wyoming in early 2012 and 2013 (Pokharel and Geerts, 2016). The second one, the 2017 Seeded and Natural Orographic Wintertime clouds: the Idaho Experiment (SNOWIE-17) (Tessendorf et al., 2018), focused on airborne seeding. Both campaigns collected rich airborne and radar observations to study cloud-microphysical processes. The orographic clouds sampled in both campaigns all produced at least some natural snowfall, i.e. there were no ice-free orographic clouds, although a few orographic cloud layers with very few ice crystals (≪1 L^{-1}) were detected in SNOWIE, and these proved to be quite seedable, at least from an aircraft (French et al., 2018). Only ground-based seeding was conducted in ASCII.

Cold-season orographic clouds are not always stratiform in nature.

Table 1
Comparison of cloud characteristics in this case study against two other ASCII-12 case studies of stratiform orographic clouds. The CIP and CDP data were collected at a flight level of 13 or 14 kft (~4.0 or 4.3 km MSL), during the NOSEED period only. The CIP concentration is in the 63–2000 μm size range only. It should be noted that the CDP data in IOP12 and IOP13 are based on limited cloud penetrations, because of instrument icing (in IOP13) and because of shallow clouds, mostly below flight level. The liquid water path (LWP) estimate is from the passive microwave radiometer at Savery (Fig. 1) and presents an IOP average.

IOP	12	13	17
date	21 February 2012	22 February 2012	3 March 2012
reference	Pokharel et al. (2014a)	Pokharel et al. (2015)	this study
CIP ice particle concentration (L^{-1})	30	17	8
CDP droplet number concentration (# cm^{-3})	86	31	125
CDP liquid water content ($g\,m^{-3}$)	0.15	0.52	0.13
LWP (mm)	0.22	0.31	0.08

Table 2
Definition of NOSEED and SEED periods for the 3 March 2012 IOP. Eight AgI generators were operating from 1930 to 2330 UTC ± a few minutes. The times are in UTC (HH:MM:SS). L refers to a ladder pattern, consisting of 5 tracks (T), as shown in Fig. 1. The UWKA flew two along-wind legs after completing two ladder patterns, thereby creating a buffer period between NOSEED and SEED (1932–2000 UTC). No such period is assumed for the instruments at Battle (MRR, Parsivel, DOW), but a ~25 min advection time between the AgI generators and Battle is applied. No DOW data is available after 22:30.

Instruments	Noseed		Seed	
	Start	Stop	Start	Stop
WCR/UWKA	18:16:28	19:32:00	20:00:52	21:16:00
UWKA cross-wind tracks	L1: T5-T1		L3:T5-T1	
	L2:T5-T1		L4:T5-T1	
MRR and Parsivel	17:30:00	19:56:00	19:57:00	22:50:00
DOW	17:30:00	19:56:00	19:57:00	22:30:00

In the presence of potential instability, the orographic lift may release that instability and give rise to embedded convective clouds (e.g., Rotunno and Houze, 2007). Sometimes, typically in post-frontal situations with significant cold-air advection, only shallow convective clouds are present over the mountains. The nature of clouds (stratiform vs. convective) affects both natural and artificially altered ice initiation, and snow growth processes, with depositional growth generally dominating in stratiform clouds and riming in convective clouds (Houze Jr, 2014). Most of the snowfall from stratiform clouds occurs on the windward side, while more snow may fall in the lee of the crest from convective clouds, especially if the instability is released rather late, close to the crest (Jing and Geerts, 2015). The seeding impact on the growth of hydrometeors is harder to isolate in convective clouds, because of natural variability, and may be found only downwind of the mountain, as shown in one ASCII-12 case study (Pokharel et al., 2014b).

Natural variability can be significant also in apparently steady stratiform clouds, as shown in two ASCII-12 case studies, making it difficult to isolate the seeding impact on stratiform precipitation also. These studies examined Intensive Operations Period #12 (IOP12) (Pokharel et al., 2014a) and IOP13 (Pokharel et al., 2015). The IOP12 and IOP13 case studies examined stratiform clouds containing high SLW content, with fewer droplets overall, but more large droplets (D > 20 μm), compared to most ASCII-12 stratiform cases. These two case studies (IOP12 and IOP13) were somewhat limited, either because of lack of flight-level particle data (as the probes became impacted by rime ice), or because the target cloud rarely reached flight level.

This paper presents a third case study of the impact of ground-based glaciogenic seeding on stratiform orographic clouds in ASCII-12. This is a study of the 3 March 2012 case (IOP17). This study is similar to IOP12 and IOP13 in that no embedded convection was present, the cloud was shallow, and it naturally produced light snowfall. This study differs from the previous studies in four important ways: firstly, this study utilizes a richer array of observations compared to the IOP12 and IOP13 case studies, and also compared to other ASCII case studies (Pokharel et al., 2014b; Chu et al., 2014; Chu et al., 2017b), which is important because it has proven difficult to tease out the seeding signal. One resource not used in the previous ASCII studies is the data from particle probes on an aircraft flying overhead, at a level corresponding with ~600 m above the mountain top. These in situ data are not expected to
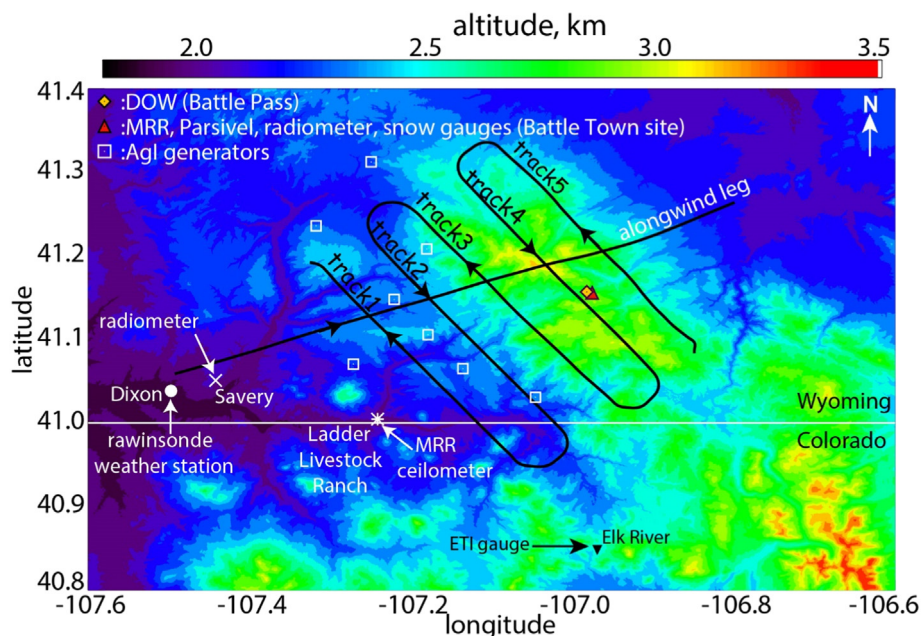

Fig. 1. ASCII-12 experimental design map, showing the location of AgI generators and instrument platforms, and UWKA flight tracks. The terrain elevation is shown in the background. The solid black lines show parts of the 3 March 2012 flight track, including the ladder pattern, with track labels (#1–5), and an along-wind leg.
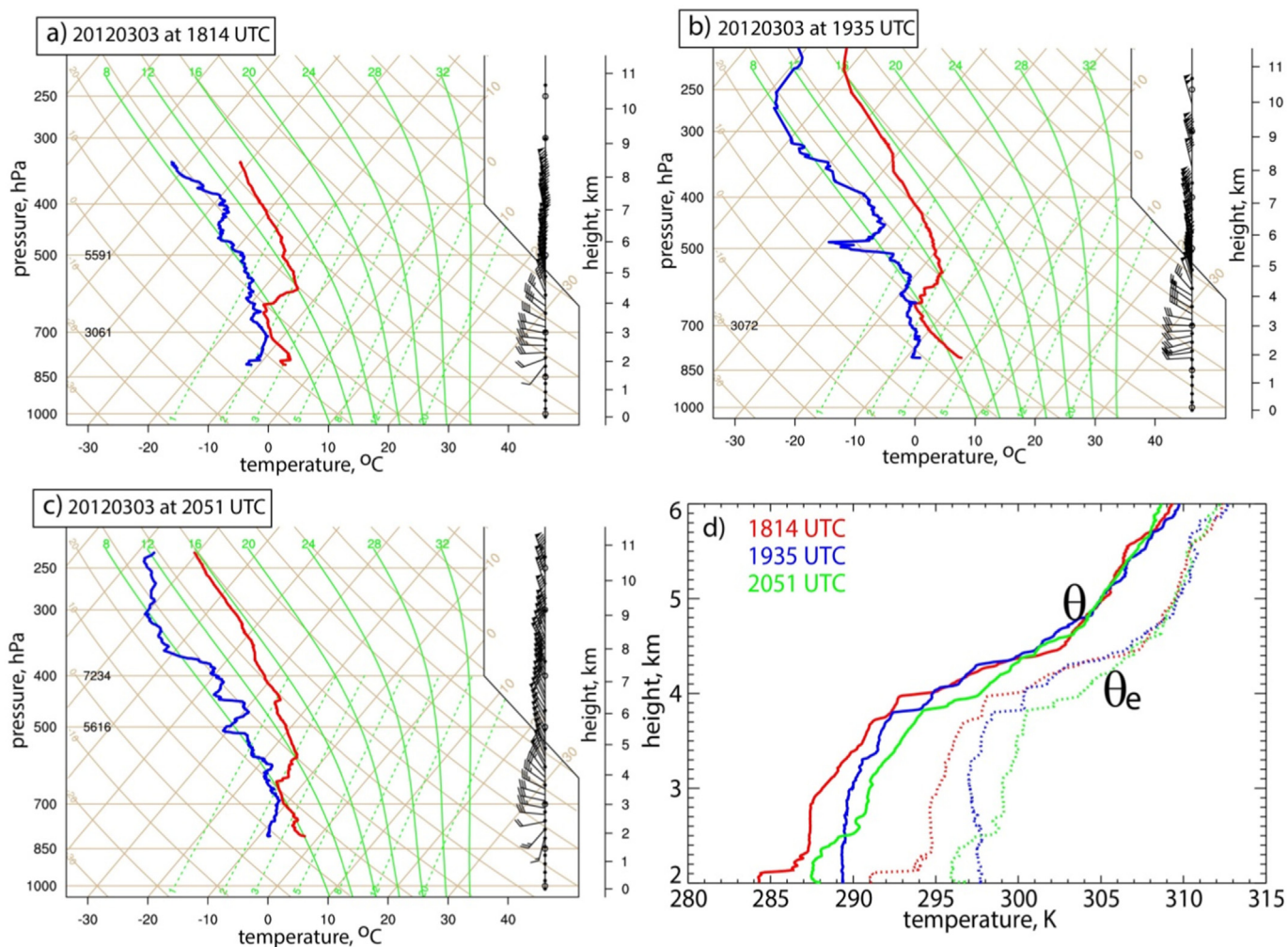
Fig. 2. Skew-T log-p display of rawinsonde data from Dixon (a) during the NOSEED period; and (b) and (c) during the SEED period, on 3 March 2012. The red lines show the temperature and the blue lines show the dewpoint. A full barb equals $5 \, \text{m s}^{-1}$ (~10 kts). (d) Vertical profiles of potential temperature θ and equivalent potential temperature θ_e for these three soundings. (For interpretation of the references to colour in this figure legend, the reader is referred to the web version of this article.)

reveal a ground-based seeding impact (since the AgI nuclei stay close to the ground, e.g. Chu et al., 2017a), but at least they characterize the orographic cloud. *As such, this is by far the most in-depth case study of all three.* Secondly, the concentration of supercooled droplets was higher in the natural cloud than in other case studies of stratiform orographic cloud (IOP12 and IOP13), according to flight-level data (Table 1). The droplets generally were small, no larger than 25 μm in diameter. Thirdly, fewer ice crystals were present in the natural cloud than in IOP12 and IOP13. And finally, many ground-based AgI generators were operated in this IOP (eight, as opposed to three in most ASCII IOPs). One of the extra generators was located further upwind of the target area, allowing more time for the impact of glaciogenic nuclei on precipitation. Several recent modelling studies (Chu et al., 2017b; Xue et al., 2016) and observational studies (Jing et al., 2016) have shown that the impact of seeding on precipitation can extend rather far downwind. The distance between the three AgI generators used in most ASCII case studies and the target mountain crest is only 15–20 km (Pokharel and Geerts, 2016). In this study, the more distant AgI generator is 25–30 km upwind of the crest.

The fundamental hypothesis underlying glaciogenic cloud seeding as a method to enhance precipitation from wintertime orographic cloud systems is that a cloud's natural precipitation efficiency can be enhanced by converting supercooled water to ice upstream and over a mountain range in such a manner that newly-created ice particles,

growing by diffusion, riming, and/or aggregation, can fall as additional snow on a specified target area. The specific hypothesis of this study is that the ground-released AgI nuclei sufficiently mix into a shallow stratiform orographic cloud to alter snow growth and snowfall. This will be examined mainly in terms of changes in radar reflectivity and also differential reflectivity in the target area, which in this case is the mountain downwind of the AgI generators. This study further examines whether a reflectivity enhancement, if it occurs, can be attributed primarily to an increase in ice particle number concentration, or to an increase in particle size.

This paper is divided in six sections. Section 2 focuses on the experimental design and instrumentation. Atmospheric conditions and measured cloud microphysics are discussed in Section 3. Sections 4 and 5 provide the seeding impact analysis based on the remote sensing measurements and in-situ measurements, respectively. The key findings are listed in Section 6.

2. Experimental design and instrumentation

The ASCII experimental design has been detailed in several studies (Geerts et al., 2013; Pokharel et al., 2014a, 2014b, 2015; Pokharel and Geerts, 2016). A composite seeding impact analysis for all 27 ASCII IOPs is presented in Pokharel et al. (2017). This study focuses on one of the IOPs, IOP17, as mentioned above. Here, the instruments and aspects
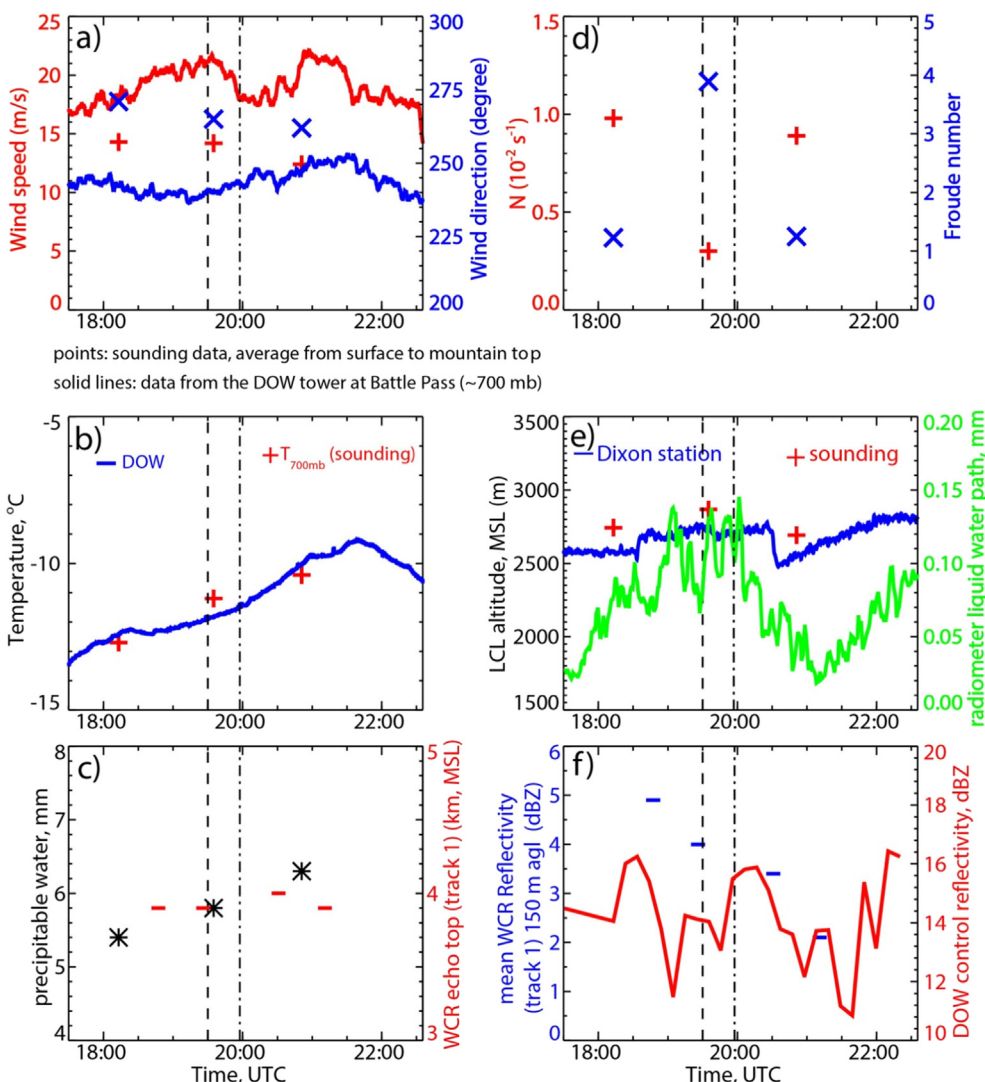
Fig. 3. Evolution of several atmospheric parameters during the course of the IOP on 3 March 2012, as measured by rawinsondes, weather station and radiometer in the upwind valley, weather station at Battle Pass (DOW), and WCR. The surface station data at Dixon and Battle Pass (DOW) have a 1 min resolution, with wind measurement at 10 m and temperature and humidity at 2 m. The vertical dashed line and vertical dashed-dotted line in all panels show the AgI generators start time and the arrival time of the AgI plume at Battle Pass (estimated from the surface wind speed), respectively.

specific to this IOP are briefly addressed. ASCII IOPs were designed to measure the cloud and precipitation at first for two hours during natural conditions (referred to as the NOSEED period), followed by a two-hour period with AgI generators in operation (SEED). The reason for this sequence was motivated by the observation that AgI nuclei typically linger, sometimes more than two hours, after the generators are shut off (Breed et al., 2014). Most of the ASCII cases include only three AgI generators, however IOP17 was a part of a Wyoming Weather Modification Pilot Project (WWMPP) randomized seeding experiment (RSE), and thus had eight AgI generators turned on for four hours (Breed et al., 2014). In this case, we define NOSEED as the ~2 h period before the start of seeding, and SEED a period of 2–3 h within this RSE, depending on the instrument and its location (Table 2). We ignore the first ½ hour of AgI seeding, as it takes time for the AgI nuclei to advect across the target area.

Measurements were made both upstream (referred to as "control") and downstream (referred to as "target") of the AgI generators, which were located in the foothills of the target mountain, the Sierra Madre in SE Wyoming (Fig. 1). The control measurements document the natural trend in orographic clouds and precipitation while the target measurements should capture the natural change plus any seeding impact

on orographic clouds and precipitation. Of course, the natural variability in the upwind control may not be exactly the same as that over the downstream target region, but they should be similar, and in fact different instruments employ different control and target regions, as discussed below.

Several ground-based and airborne platforms collected data in IOP17. The University of Wyoming King Air (UWKA) was equipped with the profiling Wyoming Cloud Lidar (WCL) and Wyoming Cloud Radar (WCR) (Wang et al., 2012), plus several in situ particle probes, i.e. a cloud droplet probe (CDP), a cloud imaging probe (CIP), a 2-D precipitating probe (2DP), plus wind, humidity, SLW and temperature sensors. The CDP, CIP and 2DP measure particles in the size range of 3–50 μm, 12.5–2000 μm, and 0.1–20 mm respectively. The first two CIP bins (< 63 μm) are excluded in the calculation of the total CIP particle concentration as such small particles are marginally resolved (Pokharel and Geerts, 2016). The CDP only provides size distribution, while the CIP and 2DP are optical array particle imaging probes.

The UWKA flew two geographically fixed "lawnmower" (or "ladder") patterns during NOSEED in an upstream direction (Fig. 1). Then, at 1930 UTC, the AgI generators were switched on (Table 2), and the UWKA flew two along-wind flight legs, allowing time for the AgI
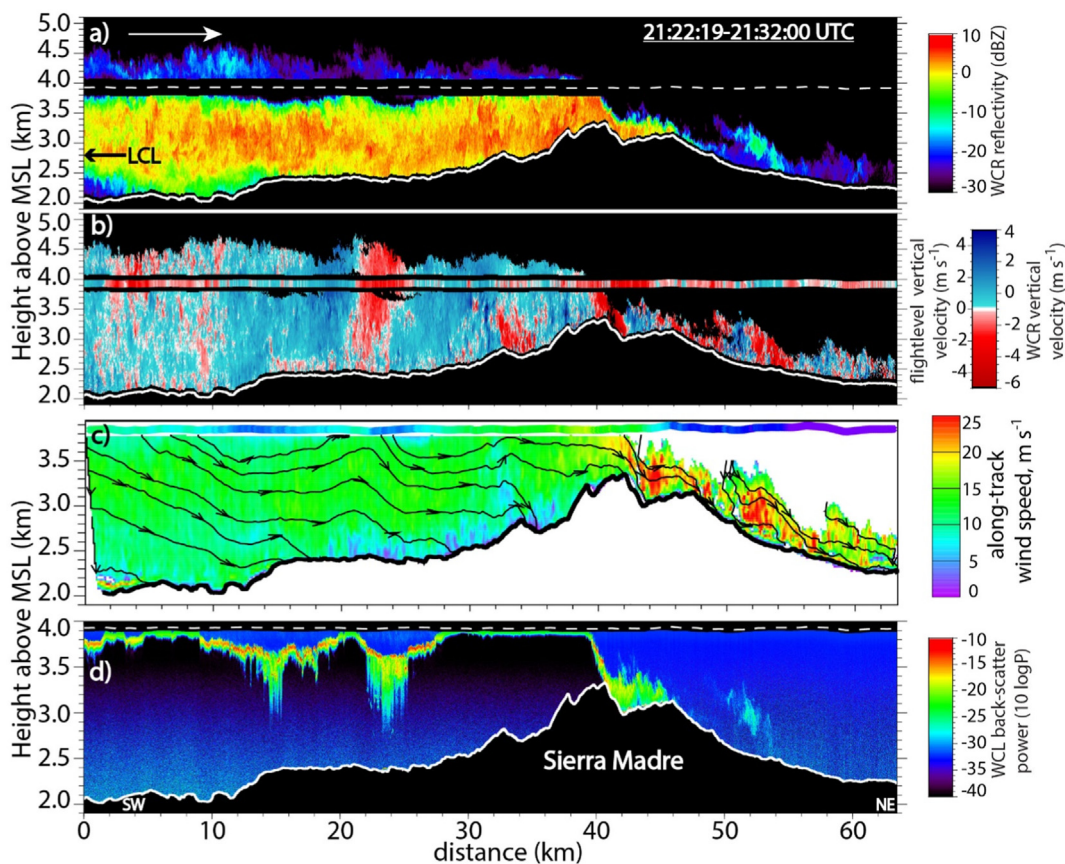
Fig. 4. WCR and WCL transect for the along-wind flight leg over the Sierra Madre shown in Fig. 1. The wind direction and UWKA flight is from left (southwest) to right (northeast). a) WCR reflectivity; b) WCR hydrometeor vertical velocity profile; also shown, at flight level, is the gust probe air vertical velocity; c) WCR dual-Doppler synthesized along-track horizontal wind below flight level and hydrometeor streamlines (black lines with arrows); also shown, at flight level, is the gust probe along-track wind speed; and d) WCL backscatter power below flight level. The dashed white line in panels (a) and (d) is the UWKA flight level, and the white line below is the terrain profile. The WCR vertical velocity scale is offset by $1 \, m \, s^{-1}$ to account for the typical fallspeed of unrimed snow. Thus blue (red) regions in panel (b) can be interpreted as updrafts (downdrafts) of air. (For interpretation of the references to colour in this figure legend, the reader is referred to the web version of this article.)

nuclei to disperse. Then the UWKA flew two more ladder patterns starting at flight track #5. These UWKA measurements compose the SEED period. Because track #1 was to the west (upstream) of all but one AgI generator (Fig. 1), WCR data from this track are treated as control. (Any contamination from the one AgI source further upstream is ignored as in this case the cloud base was well above the elevation of that source.) The four other tracks (#2–5) are downstream of most AgI generators, thus these data are treated as target. The Sierra Madre topography has to be considered as well: tracks #2–3 are located upstream of the crest, track #4 is close to the crest, and track #5 is in the lee.

The key instruments on the ground are the X-band dual-polarization Doppler-on-Wheels (DOW) radar (Wurman et al., 1997), a Cloud Particle Imager (CPI, Lawson et al., 2006), a profiling 24-GHz Micro Rain Radar (MRR), a Parsivel disdrometer (Löffler-Mang and Joss, 2000; Yuter et al., 2006), and an Environmental Technology Inc. (ETI) precipitation gauge. The DOW was located at Battle Pass (Fig. 1) and the other instruments were mounted on a scaffold structure sheltered by trees at a site (referred to as Battle Town site) some 500 m downwind of the DOW. The DOW completed full volume scans every 8 min, and thus provided continuous 3D measurements, whereas WCR reflectivity data were collected only in a vertical transect along the flight track (twice during NOSEED and twice during SEED). On the other hand, DOW data were generally not available very close to the ground, notwithstanding

the −1° minimum elevation angle, on account of ground clutter and beam blockage. But Battle Pass had excellent views towards the AgI generators on the SW (upwind) side, and towards the east (lee) side, thus covering both control and target areas. The DOW control and target regions will be defined in Section 4.3 below. Details of the DOW data processing for ASCII can be found in Jing et al. (2015). The DOW system includes a weather station with 10 m wind and 2 m temperature and humidity.

Fresh snow samples were collected regularly at Battle Town site, to analyze the concentration of silver (Ag) and other trace elements in falling snow. The Battle town site was located roughly downwind of several AgI generators during IOP17, thus its data serve as target measurements. A second MRR, whose data are used as a control measurement, was operated at Ladder Livestock ranch (Fig. 1) upstream of the AgI generators. After data reprocessing following Maahn and Kollias (2012), the lowest data level was 450 m AGL for the MRR at Battle Town site, and 700 m for that at the Ladder Livestock ranch. The ASCII instrument network further included a ceilometer, a passive microwave radiometer, an automated weather station, and radiosondes (Pokharel and Geerts, 2016). The radiometer, a multi-angle dual-frequency system located at Savery (Fig. 1), is used to estimate cloud liquid water path (LWP) over the Sierra Madre, as it was pointed at an angle just above the topography. Three GPS radiosondes were released from Dixon (Fig. 1) during this IOP.
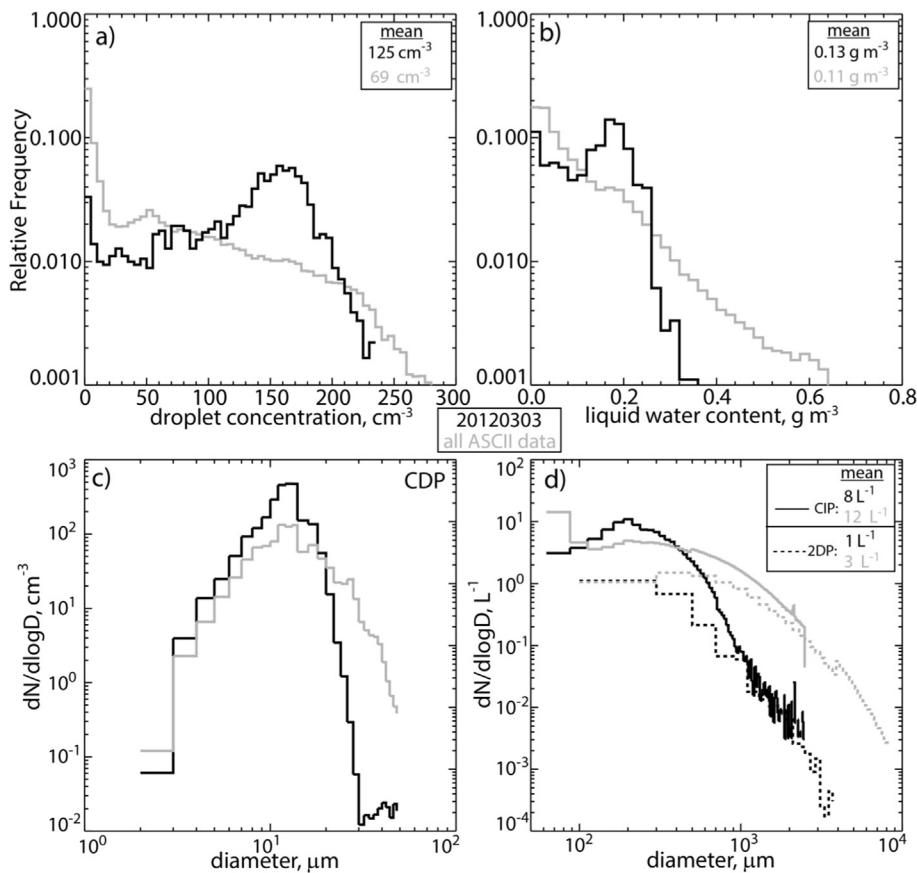
Fig. 5. Droplet and ice concentrations measured at flight level during the NOSEED period by the CDP, CIP and 2DP during IOP17 (black line) and from all ASCII data over two mountain ranges in southern Wyoming (gray line). a) probability distribution of droplet concentration, b) probability distribution of LWC, c) mean droplet size distribution measured by the CDP, and d) mean ice particle size distribution measured by the CIP and 2DP.
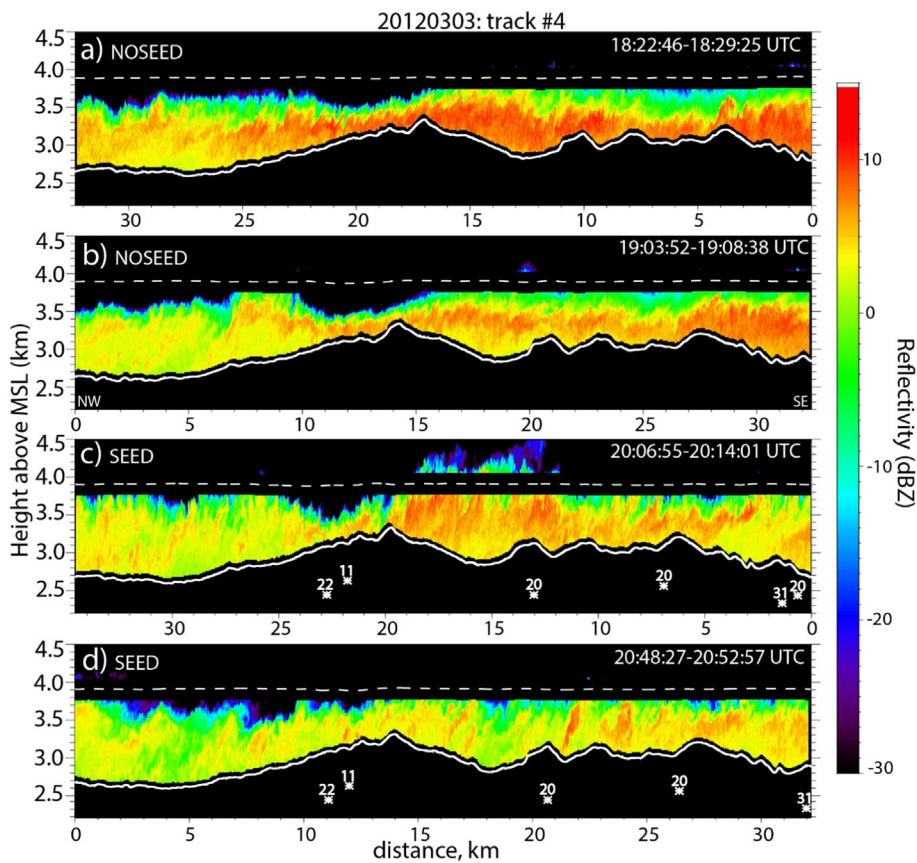

Fig. 6. Example WCR reflectivity transects, collected along flight track #4 (Fig. 1) on 3 March 2012. All transects are from NW (left) to SE (right), the direction of the low-level shear (Fig. 2). The upper two transects were flown during NOSEED, the lower two transects during SEED. The asterisks in third panel show the location and actual elevation of the six AgI generators (into the page) projected on this transect, following the mean low-level wind. The distance (km) to those generators along the low-level wind is shown next to each asterisk. The actual terrain is shown by the white line and the UWKA flight level (3.9 km, MSL) is shown by the white dashed line in all panels.
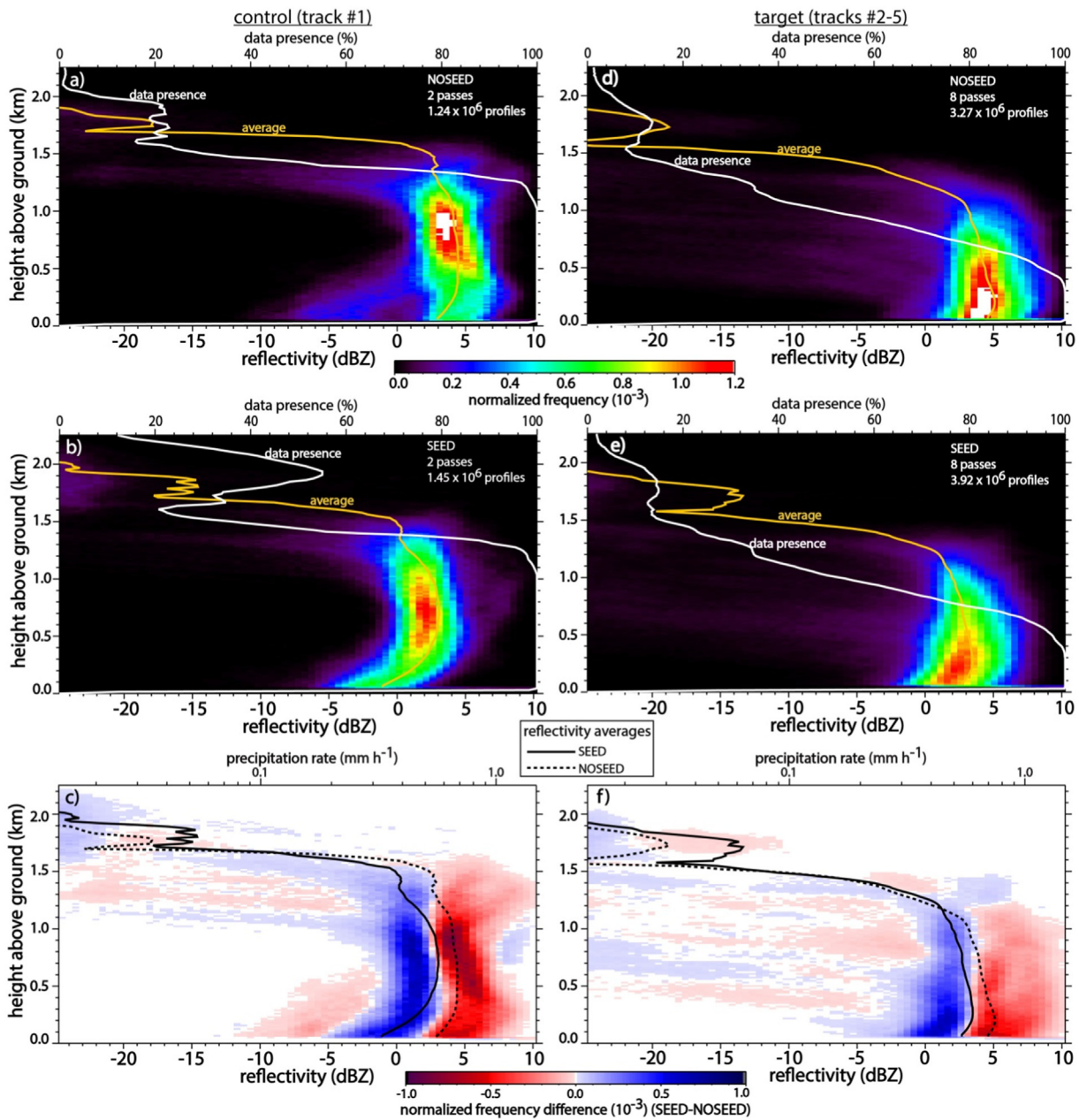
Fig. 7. Normalized frequency by altitude diagrams (FADs) of WCR reflectivity (top panels) and vertical velocity (middle panels) for the 3 March 2012 flight. The left panels apply to track #1 (control), the right panels to the four tracks downwind of the AgI generators (target). Also shown in the top panels are the mean reflectivity profile (orange lines) and the "data presence" profile, i.e. the percentage of WCR range gates with radar echo as a function of height (white line). Also shown in the middle panels are the average vertical velocity profile (orange line) and average profiles during the NOSEED (dashed line) and SEED (solid line) periods. c) & f) the reflectivity *difference* FAD (SEED – NOSEED), with the average reflectivity profiles for the two periods (black lines).
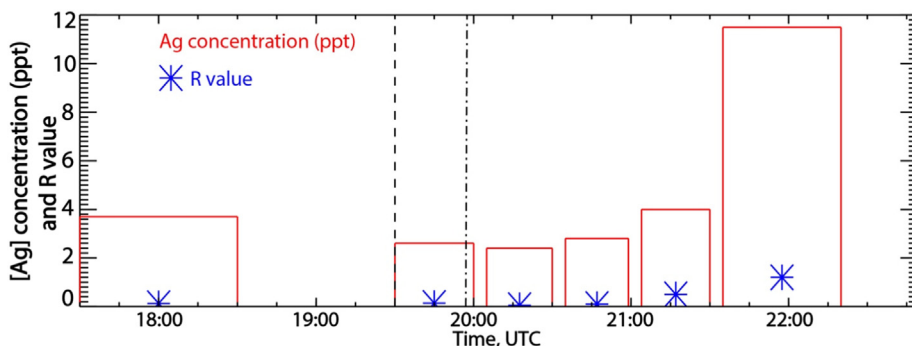

Fig. 8. Time series of silver (Ag) concentration in parts per trillion (ppt) from three fresh snow samples collected during the 3 March 2012 IOP at Battle Town site. The width of the histogram shows the duration of snowfall collected. The vertical dashed line shows the AgI generators start time. The dashed-dotted line is the estimated time of the AgI plume arrival at Battle Pass, based on surface wind speed. It separates the NOSEED and SEED periods.
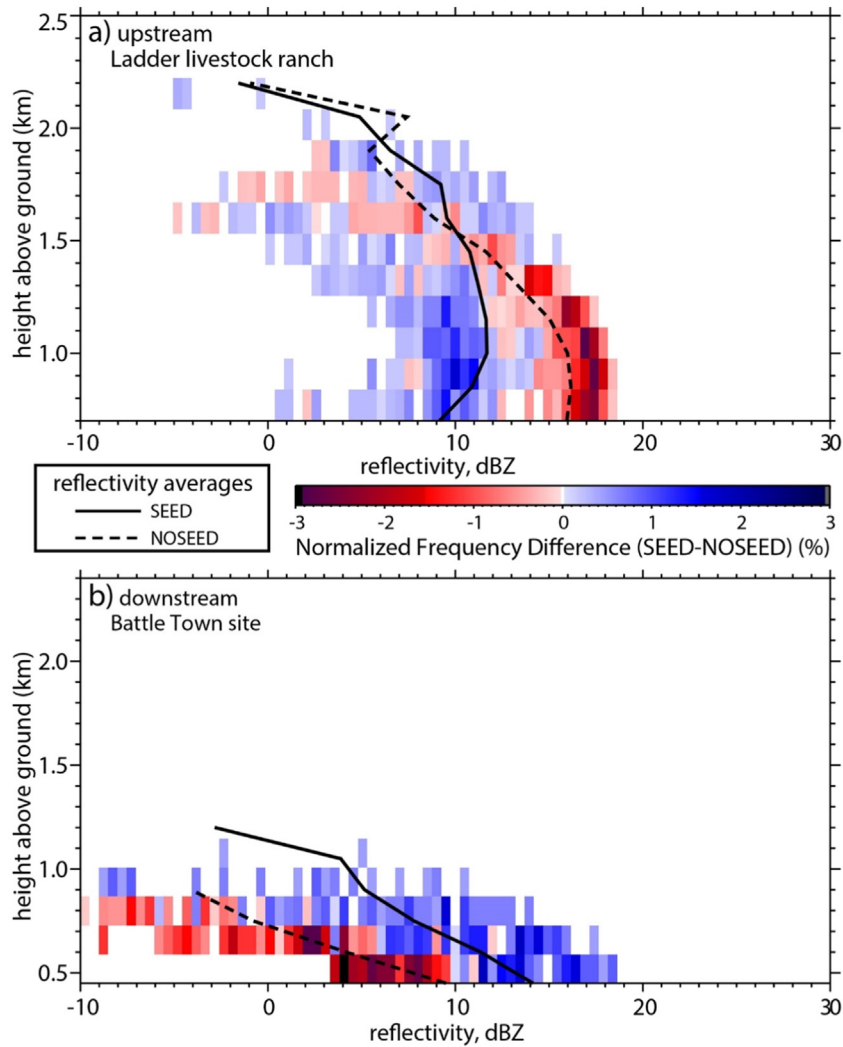
Fig. 9. The normalized reflectivity difference FAD for [SEED – NOSEED] for a) the upstream MRR (control), and b) the downstream MRR (target). The NOSEED and SEED periods are defined in Table 2.

3. Atmospheric conditions and cloud characteristics

3.1. Synoptic conditions and atmospheric profiles upstream of the mountain

IOP17 on 3 March 2012 occurred in the wake of a deep upper-level ridge passing over Wyoming. A northwesterly jet, located over NE Wyoming, produced upper-level subsidence. At low levels, very cold air covered the central part of the United States, with much warmer air to the west. The northwesterly flow transported water vapor from the Pacific Ocean into the region, which resulted in orographic precipitation over a series of mountain ranges from the Cascades to the Sierra Madre. Steady, light snowfall occurred over the Sierra Madre during the IOP17.

The balloon soundings indicate a shallow layer near ice saturation up to approximately 4.0 km AGL (immersing the Sierra Madre which peaks at 3.36 km MSL or 670 mb), an inversion up to ~4.5 km AGL, and warm, dry air aloft (Fig. 2). The wind gradually veers from southwesterly near the surface to northwesterly at the top of the shallow moist layer. Near mountain crest level, the wind is westerly at 30–35 kts. The sounding based lifting condensation level (LCL) is about −9 °C, cold enough for AgI-based ice nucleation (Demott, 1999). The cloud top temperature is about −16 °C. As will be shown below, this was not cold enough for extensive natural ice initiation, in fact numerous liquid droplets were observed near cloud top. The cloud base height in all

three soundings was below Battle Pass level (3000 m), assuming either the surface-based or the mixed-layer (500 m deep) LCL. Thus, the strong orographic flow (and thus well-mixed boundary-layer), the low cloud base, the cloud temperature range, and the lack of ice clouds aloft (shown also in the WCR reflectivity transects, discussed in Section 3.3) all imply suitable conditions for ground-based AgI cloud seeding.

In order to tease out the seeding signal from a non-simultaneous comparison (SEED vs NOSEED), steady conditions are needed. The three soundings were indeed quite similar with a shallow cloud layer strongly capped near 4.0 km MSL (Fig. 2d).

3.2. Storm conditions and evolution during the IOP

In order to further characterize the IOP17 storm conditions and to quantify natural changes during the duration of the IOP, we plotted a large array of data against time in Fig. 3. The most significant change is the observed warming by ~4 K during the IOP (Fig. 3b), due to a combination of warm-air advection (consistent with veering winds with height, Fig. 2) and daytime surface heating (local solar noon is at 19:04 UTC). The wind speed and direction are rather steady (Fig. 3a). The wind is stronger in the Battle Pass gap (20 m s^{-1}) compared to the average wind (15 m s^{-1}) measured by the soundings from surface to mountain top level (Fig. 3a). The bulk Brunt-Vaisala frequency *N*, calculated from the surface in Dixon (in the valley) to mountain top level,
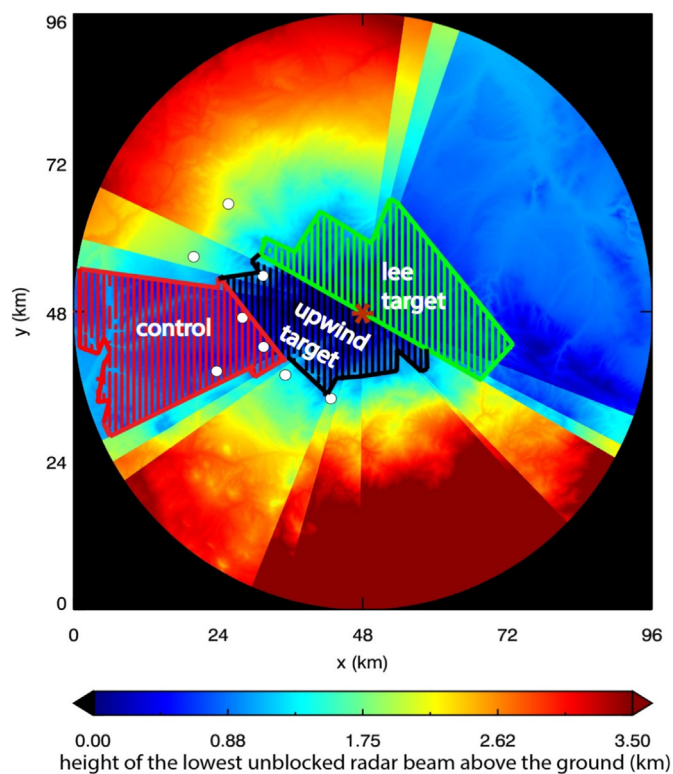
Fig. 10. Height (km AGL) of the lowest unblocked beam AGL from the DOW radar, located at Battle Pass (Fig. 1). Also shown are three vertically hatched regions used in the analysis of the seeding impact: the upstream control region (red hatching), the "upwind target" region (black) upwind of the mountain crest, and the "lee target" region (green) in the lee. The red asterisk shows the DOW location and white circles are the AgI generators. (For interpretation of the references to colour in this figure legend, the reader is referred to the web version of this article.)

indicates stratified conditions ($N \sim 0.01\,\mathrm{s}^{-1}$) (Fig. 3d), except for the second sounding, which reveals close to dry-neutral conditions in the boundary layer and near moist-neutral conditions higher up in the moist layer (Fig. 2b, d). The bulk Froude number[2] Fr is slightly larger than unity (1.0) for the first and third soundings while for the second sounding it has a larger value ($Fr \sim 4$). Excluding the shallow valley inversion in the first and third soundings (Fig. 2d), $Fr > 2$ in all three soundings, suggesting that the low-level flow was unblocked and crossed the mountain crest during this IOP. The LCL (cloud base), estimated from the soundings and from Dixon weather station (Fig. 3e), generally is above the elevation of the AgI generators (2.4–2.6 km MSL) yet below that of Battle Pass (3.0 km MSL). This suggests that the released AgI nuclei enter into the cloud before crossing the mountain crest.

The presence of SLW in clouds over the Sierra Madre was confirmed by the radiometer at Savery (Fig. 3e), however the magnitude is about 0.1 mm (100 g m^{-2}), rather low. If we assume a cloud depth of 1 km, then the vertically averaged LWC would be 0.10 g m^{-3}. This is close to the measured average LWC (0.13 g m^{-3}) by the CDP at flight level. The radiometer LWP is higher during NOSEED compared to SEED (Fig. 3e), while the precipitable water (integrated water vapor calculated from three soundings) shows the opposite (Fig. 3c). The mean near-surface WCR reflectivity decreases along track #1 (the control track) during the IOP (Fig. 3f), but the DOW reflectivity in its control region and the WCR

_____

[2] The Froude number is calculated as $Fr = U/(NH)$, where U is the surface-to-mountaintop mean wind speed and H is the height of the mountain above the upwind plains.

echo top height both remains steady (Fig. 3c and f).

3.3. Orographic cloud and precipitation characterization

The persistent orographic cloud in IOP17 is depicted well in the along-wind flight transect across the Sierra Madre (Fig. 4). The WCR echoes in this transect, flow just after the SEED period, are < 2 km deep on the upwind side (Fig. 4a). The air layers containg the stratiform cloud are squeezed over the mountain. Strong subsidence near the crest (Fig. 4b) causes the ice crystals to sublimate rapidly in the lee, except near the surface. The upward/downward (positive/negative) vertical velocity dipoles are associated with the terrain (Fig. 4b); the flight-level vertical velocity matches well with the WCR measured vertical velocity near flight level, with the assumption of a particle fall speed of 1 m s^{-1}. The WCR dual-Doppler along-track wind speed is shown in Fig. 4c. The hydrometeor streamlines (which are tangential to the 2D wind at any location) indicate wave-like motion upwind, and a downslope windstorm on the lee side (Fig. 4c). There are some scattered ice crystals above flight level, detectable by WCR, but the liquid cloud top remains mostly below or at flight level. This cloud contains a high concentration of SLW droplets, based on the high value of lidar backscatter power just below flight level on the upwind of the crest (Fig. 4d). The SLW diminishes immediately on the lee from the crest due to deep subsidence evident at flight level (Fig. 4d). The lee side shallow WCR reflectivity could be associated with blowing snow (Geerts et al., 2015).

Even though the orographic cloud was shallow, the UWKA (flying at a constant flight level of 13 kft or 3962 m) penetrated the cloud tops frequently during different ladders on the upwind side of the Sierra Madre (Tracks #1–4). The average droplet concentration measured at flight level over the target mountain during NOSEED (Tracks #1–4) is about 125 cm^{-3} with a maximum value just over 200 cm^{-3} in a deep updraft (Fig. 5a). The mean droplet concentration measured on IOP17 is almost twice the mean value for all ASCII IOPs [~70 cm^{-3}, Pokharel and Geerts, 2016]. The average flight level LWC (where liquid is present) is 0.13 g m^{-3} (Fig. 5b), a typical value for winter orographic clouds in Wyoming (Pokharel and Geerts, 2016; Politovich and Vali, 1983). The CDP droplet size distribution reveals a mode diameter of about 12 μm (Fig. 5c), which also is typical for such clouds, even though very large supercooled droplets were observed in one ASCII-12 case (Pokharel et al., 2015). The (natural) ice concentration near cloud top is quite low, < 10 L^{-1} (Fig. 5d). This may be attributed to the lack of ice multiplication (splintering), since this cloud lacks large droplets and is too cold. The ice concentration measured in IOP17 is smaller than the ASCII mean value (Fig. 5d). The huge difference between the droplet and ice particle concentrations (4 orders of magnitude) suggests that additional ice nuclei may enhance snow growth by diffusion. In short, the measured cloud appears to be a good target for glaciogenic seeding.

4. Seeding impact detection: radar reflectivity

Three different radar systems (WCR, MRR, and DOW) are used to examine how seeding may affect snowfall in this IOP. The SEED measurements are compared against NOSEED measurements in both control and target regions, as in previous studies (Pokharel et al., 2017). The three radar systems differ in terms of frequency (and thus sensitivity to hydrometeors of different sizes), viewing angle (vertical vs. quasi-horizontal), and spatial coverage (and thus definition of control and target regions). Moreover, the SEED and NOSEED periods are not exactly the same (Table 2), so the analyses from the three radar systems should be seen as complementary.

The relationship between cm-wave reflectivity and snowfall rate is well-established (e.g., Wolfe and Snider, 2012). While mm-wave radar reflectivity cannot be used to measure heavy snowfall rate (it saturates at ~25 dBZ), it correlates strongly with snowfall rate when particles are small, as evidenced by studies using particle scattering models (Matrosov, 2007) and observations (Pokharel and Vali, 2011; Matrosov
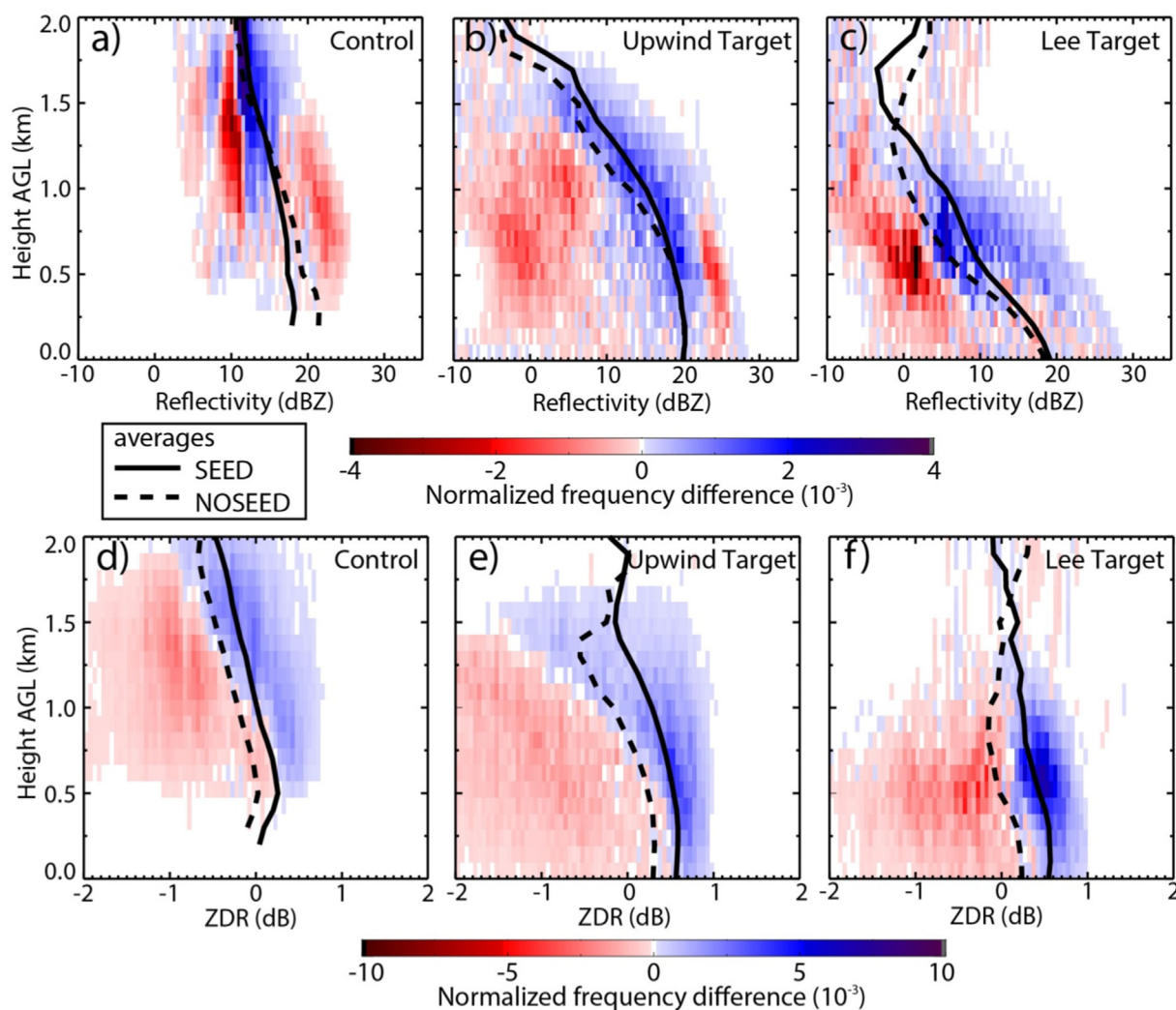
Fig. 11. The upper panels show the DOW radar reflectivity difference FADs (SEED – NOSEED) measured in the (a) control region, (b) upwind target region, and (c) lee target region. The lower panel shows the DOW differential reflectivity (ZDR) difference FADs (SEED – NOSEED) measured in the (d) control region, (e) upwind target region, and (f) lee target region.

et al., 2009; Rasmussen et al., 2003). IOP17 has a peak reflectivity of just 10 dBZ, and most ice particles are < 1 mm in diameter (Fig. 5d).

4.1. Wyoming Cloud Radar

WCR reflectivity has been used before to examine the impact of glaciogenic seeding on snowfall rate, both in case studies (Geerts et al., 2010; Pokharel et al., 2014a, 2014b, 2015) and in a composite data analysis (Pokharel et al., 2017). In none of the cases, a clear seeding signature in WCR reflectivity transects (i.e., a plume of increased reflectivity) emerged downwind from the AgI generators. The WCR reflectivity transects from track #4 are shown in Fig. 6. The first two transects are from NOSEED, and the AgI generators had been on for at least 1 h for the other transects. The projected location, along-plume distance as well as the actual elevation of the six AgI generators are shown in third and fourth panels (Fig. 6c-d). The projection uses the average wind direction below mountain top level from the nearest sounding (Fig. 2). The remaining two AgI nuclei plumes did not cross track #4 (Fig. 1). The reflectivity is highest during the first transect and decreases steadily in later transects, consistent with track #1 data (Fig. 3f), implying that the storm was weakening during the IOP. No clear local reflectivity increase (seeding signature) near the projected locations of the AgI plumes is observed during SEED.

Since an obvious seeding signature is not apparent in individual WCR reflectivity transects, the reflectivity data are analyzed in composite sense, and the analysis focuses on the change [SEED – NOSEED] in the target area against the same change in a control area, also as in previous case studies (Pokharel et al., 2014a, 2014b, 2015). Flight tracks #2–5, which are downwind of the AgI generators, are treated as *target* and track #1 is treated as *control* (Fig. 1). Track #1 may not be completely untreated since it is ~6 km downwind of one AgI generator, but it certainly is less treated. It could be argued that track #2 should be part of the control group, since it takes some time (and advective distance) for AgI to grow ice crystals. Three recent seeding impact modelling studies indicate an increase in low-level reflectivity starting around 7–9 km downwind of the AgI generators and peaking at 17–19 km downwind, for winter storms in the same region as the case examined here. These studies examine a shallow convective storm over the Sierra Madre (Chu et al., 2017a), and two separate shallow stratiform storms over an adjacent mountain, the Medicine Bow range (Xue et al., 2016, and Chu et al., 2017b). Track #2 is a mere 3 km downwind of an array of three AgI generators that is aligned with the flight track (Fig. 1). The above-mentioned model results suggest that the strongest impact on reflectivity should be expected along track #4, ~17 km downwind of the generator array.

The composite reflectivity data are shown as frequency by altitude diagrams (FADs) (Yuter and Houze, 1995) in Fig. 7, for control and target regions, and for NOSEED and SEED periods. These diagrams
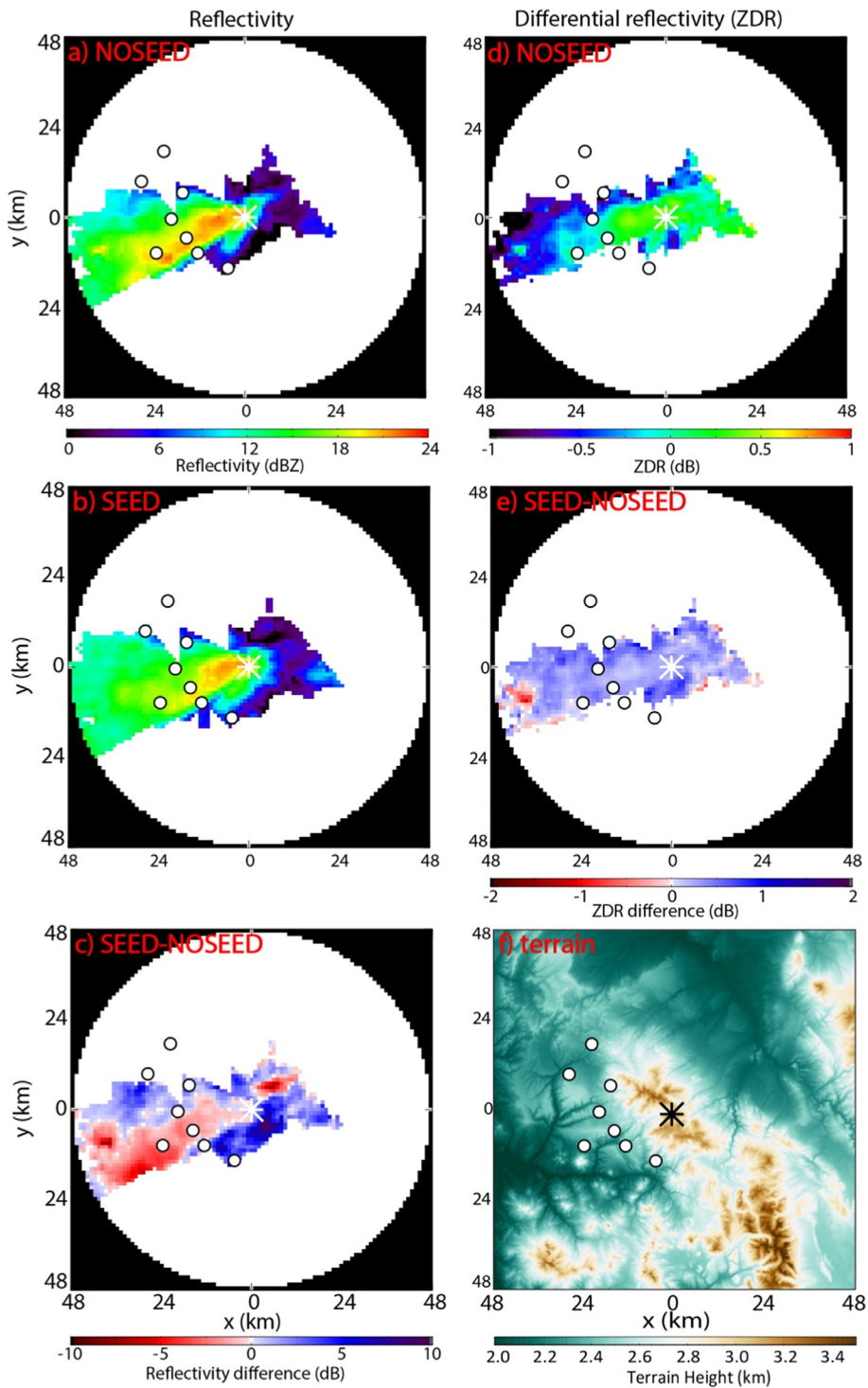
Fig. 12. The left panels show the average DOW reflectivity below 1.5 km AGL during a) NOSEED, b) SEED, and c) the mean reflectivity difference between these two periods. The two upper right panels show the average ZDR below 1.5 km AGL during d) NOSEED and e) the mean ZDR difference (SEED – NOSEED). The lower right panel f) shows the terrain map. In all these maps, the white circles are the AgI generators and the asterisk locates the DOW.

show the normalized frequency of a reflectivity value at certain height above the terrain and at certain bin. The WCR reflectivity FADs confirm the higher reflectivity during NOSEED compared to SEED both in control and target regions, i.e. the storm was weakening during the 3 h period. *The decrease in reflectivity is larger in control track* (Fig. 7c) compared to the target tracks (Fig. 7f), especially near the ground. If we assume that the natural trend is the same in target and control regions, and recall that the control track shows natural changes only while the target tracks show natural changes plus any seeding effect, then we find

a positive impact of seeding on reflectivity and thus on snowfall rate. This will be discussed in more detail in Section 4.5.

4.2. Micro-Rain Radars

Two MRRs were deployed during IOP17. One MRR was located upwind of the AgI generators (control) and the other was located downwind at Battle Town site (Fig. 1). Measurements at Battle Town site can be treated as "target" only if the site was within an AgI plume
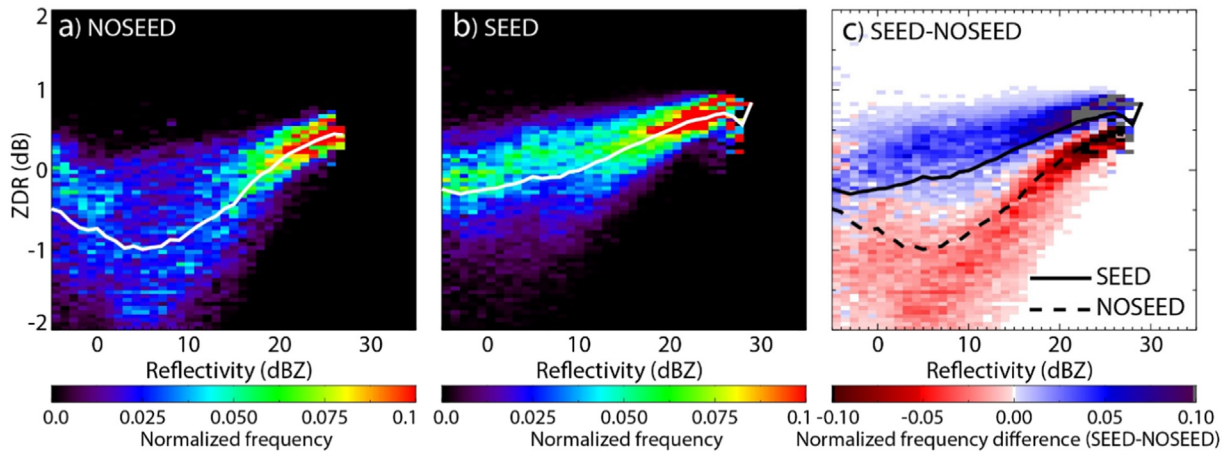
Fig. 13. Normalized frequency of reflectivity (*Z*) by ZDR for the target (upwind plus lee) region, during (a) the SEED period and (b) the NOSEED period in IOP12. The frequency difference (SEED – NOSEED) is shown in (c). Only points within 1.5 km AGL are included in the count. The white lines in (a) and (b) represent the average ZDR for any *Z* value. They are repeated as black lines in (c).
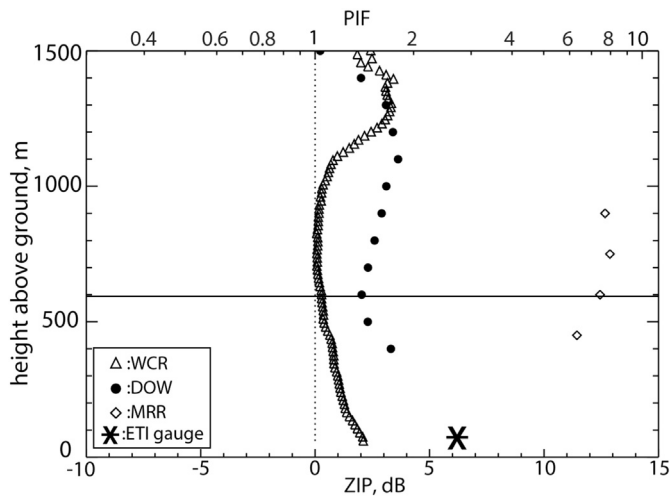

Fig. 14. Vertical profiles of ZIP/PIF (defined in the text) for three radar systems and gauge-estimated PIF. The upwind and lee target regions are combined for the DOW. The vertical dotted line separates a positive effect to the right from a negative effect to the left. The horizontal solid line is the WCR-derived average PBL depth.

during SEED. The WSW surface wind directions observed at various locations, including at Battle Pass, suggest that the AgI plumes from at least one of the eight active AgI generators reached Battle Town site. The channeling of the flow (and AgI plumes) into Battle Pass makes this assessment even more likely.

Snow samples collected at Battle Town site were analyzed in a lab for concentrations of Ag (silver) and four other naturally co-varying trace elements. The ratio of Ag concentration over the concentration of these other trace elements [referred to as the R-value, Pokharel et al., 2014b] is shown in Fig. 8 for six snow samples collected during IOP17. These other trace elements are Rb (Rubidium), Ba (Barium), Sr (Strontium) and Ce (Cerium). They naturally correlate well with Ag, as their variation is due to varying atmospheric mineral aerosol loads. An R-value larger than 1 indicates that the enhancement of Ag concentration must be due to AgI seeding. Both Ag concentration and R-value were not significantly higher until the penultimate snow sample, which includes snow falling near the end of the UWKA SEED period (Table 2). The last snow sample, collected around 2200 UTC after the UWKA had left the scene, contains strong evidence of artificial Ag in the falling snow. This is consistent with previous studies that the AgI plume (or Ag-containing snowflakes) may take as long as two hours to reach

Battle Town site (Pokharel et al., 2014a, 2014b, 2015), even though the calculated travel time for the AgI nuclei is about 30 min, based on the mean wind. This confirms that the AgI plume reached Battle town site, but rather late in the SEED period, which ends at 2250 UTC for instruments at that site (MRR and Parsivel, see Table 2).

The MRR reflectivity difference FADs from the control site is consistent with WCR measurements: the storm was weakening (Fig. 9a). And the positive seeding impact is far more obvious for the MRR than for the WCR, with higher reflectivity during SEED (compared to NOSEED) over the target MRR (Fig. 9b), notwithstanding the generally weakening storm. The difference between MRR-based and WCR-based seeding impact probably is because SEED lasted 1.5 h longer for the MRR (Table 2), and snow trace element analysis (Fig. 8) suggests that that the target MRR is most impacted by seeding during that last 1.5 h. The MRR reflectivity at Battle Town site is so shallow on account of the sudden subsidence in the lee of the Sierra Madre crest (Fig. 1), evident in WCR data (Fig. 4b) and also MRR Doppler velocity data (not shown).

4.3. DOW radar

The DOW provides a full volume of 3D data covering both target and control regions across the Sierra Madre. As mentioned before, low-level coverage from Battle Pass is limited to the NW and S of the radar, because of terrain blockage, but the low-level views along the wind direction are excellent (Fig. 10). The DOW data are partitioned into three regions for the purpose of examining the seeding impact (Fig. 10). This approach is similar to Jing et al. (2015), Pokharel et al. (2015), and Pokharel et al. (2017), but in this case, there are eight AgI generators. The region upwind of most AgI generators, where the lowest unblocked DOW beam is not higher than 1.0 km above the terrain, is treated as *control region*. This region has almost no data below ~500 m AGL (after ground clutter removal), because of its distance from the radar. Two target regions are distinguished, as in previous studies: the *upwind target* is downstream of most AgI generators, but upstream from the mountain crest; and the *lee target* is downstream of the mountain crest. The boundaries of the two target regions are further defined by the requirement that the lowest unblocked DOW beam cannot exceed 1 km AGL.

The DOW reflectivity (*Z*) and differential reflectivity (ZDR) data are composited for two periods (NOSEED and SEED) and the above-mentioned three regions in Fig. 11. Also shown in this figure are the resulting reflectivity and ZDR *difference* FADs [SEED – NOSEED]. Recall that the DOW SEED period ends rather late, almost as late as the MRR SEED period (Table 2). We see some basic orographic changes in mean reflectivity profiles, i.e. an increase in low level reflectivity from the
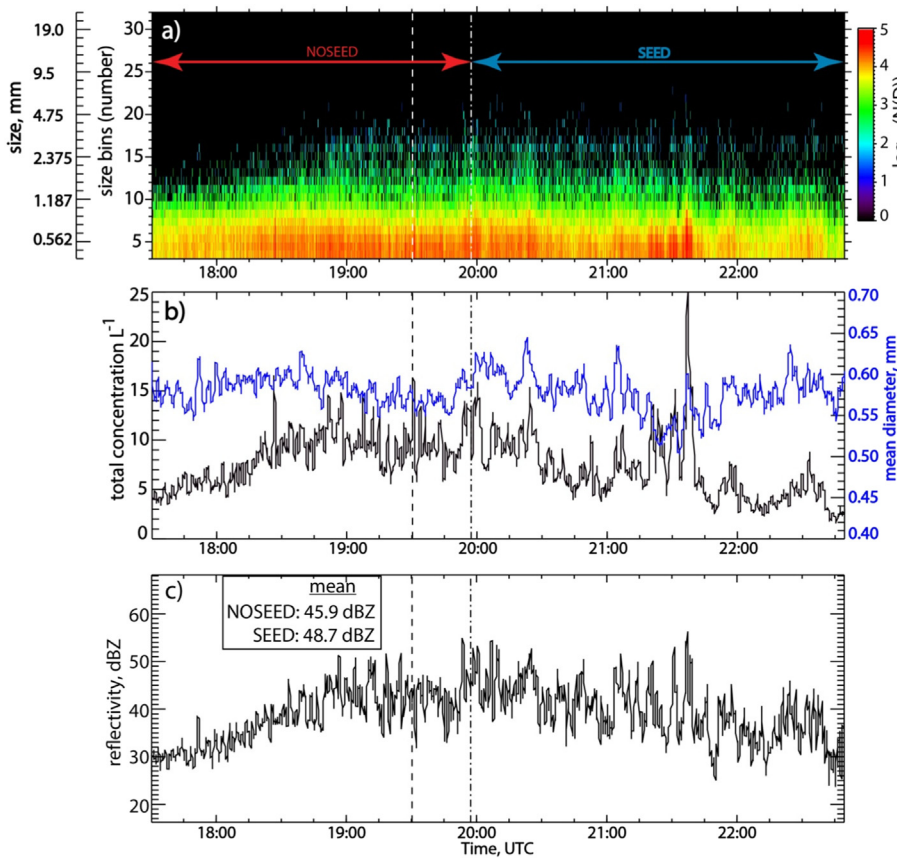
Fig. 15. Time series of Parsivel disdrometer measurements at Battle Town site: (a) snow size distribution; (b) total snow concentration (black line) and mean diameter (blue line), and (c) calculated reflectivity based on the Parsivel size distribution. The vertical dashed and dashed-dotted lines in all panels are the AgI generators start time and the estimated arrival time of the AgI plume at Battle Pass, respectively. (For interpretation of the references to colour in this figure legend, the reader is referred to the web version of this article.)

foothills (control) to mountain (upwind target), and a decrease from upwind to lee target areas at low levels (below 1.5 km AGL) (Fig. 11a, b and c). The mean DOW reflectivity decreases significantly during the IOP in the control region (Fig. 11a), consistent with the WCR and MRR findings: the storm is weakening. Yet it remains unchanged or increases from NOSEED to SEED periods in both target regions (Fig. 11b and c), *suggesting that the natural storm weakening is at least offset by seeding*. This positive seeding impact is slightly more pronounced at greater fetch, i.e. in the lee target area.

Differential reflectivity (ZDR) can be negative for ice crystals that tend to be oriented vertically, but higher ZDR values (above 0 dBZ) imply larger, more horizontally oriented scatterers, mostly likely aggregates which generally have ZDR values between 0 and 2 dB (e.g., Kumjian, 2013). Because seeding increases the number of ice crystals, it also increases the chances of aggregation, so it is plausible that seeding will increase ZDR (Jing et al., 2015).

The ZDR values in IOP17 are distributed around 0.0 dB in the control region (Fig. 11d) and slightly higher in the target regions, around 0.3–0.6 dB (Fig. 11e and f). These values are similar to those in other stratiform cloud cases in ASCII (Jing et al., 2015). The ZDR difference FADs show an increase in ZDR value with time during the IOP in all three regions (Fig. 11 d, e and f), thus this is a natural trend, but the increase in ZDR during SEED is larger in the target regions. This is consistent with an increase in ice particle aggregation, which is also observed both at flight level and at the ground, as will be discussed in Section 5 below.

To examine the spatial distribution of DOW Z and ZDR over the target and control areas, we map out their average values below 1.5 km AGL in Fig. 12. The orographic effect of precipitation enhancement towards the crest is clearly observed in both NOSEED and SEED periods (Fig. 12a and b). ZDR is mostly negative in the control region during NOSEED, due to small, mostly vertically oriented ice crystals, but becomes mostly positive towards the crest, due to natural aggregation or

predominance of dendrites (Fig. 12d). The storm generally weakens in the control area, resulting in mostly negative [SEED-NOSEED] Z values (Fig. 12c). These values are mostly positive downwind of the AgI generators, esp. the southernmost generators. The small-scale structure of the [SEED-NOSEED] Z field (Fig. 12c) probably is not very meaningful since the Z field itself has transient echoes that may dominate in the rather short-term averages shown here. Certainly, there is no clear "signature" of enhanced Z downwind of individual generators. The ZDR field shows a positive trend during IOP17, mainly in the target regions (Fig. 12e), consistent with Fig. 11.

Finally, we examine the variation of ZDR for a given value of Z in the target region (Fig. 13). The question is: for a given Z (and thus a given size of the largest snow particles in a DOW resolution volume), what is the ZDR distribution? During NOSEED the ZDR spread is rather broad for a given Z, indicating a variety of particle orientations. During SEED ZDR becomes more narrowly distributed and increases monotonically with Z, i.e. larger particles are more horizontally oriented, as expected from aggregation (Fig. 13b). *The ZDR is significantly larger during SEED for any Z value* (Fig. 13c), indicating that *a particle of a given size is more likely to be an aggregate (higher ZDR) during SEED*. This is consistent with the hypothesis that seeding enhances the ice crystal concentration and thus the chances for aggregation. Seeding does not systematically affect the co-polar correlation coefficient (ρ_{hv}), for any value of Z (not shown).

4.4. Profiles of radar reflectivity change

All three radar systems show that this snowstorm was weakening over the Sierra Madre during the IOP. To isolate the glaciogenic seeding impact, we compute a double difference, as in Pokharel et al. (2014a, 2015, 2017):
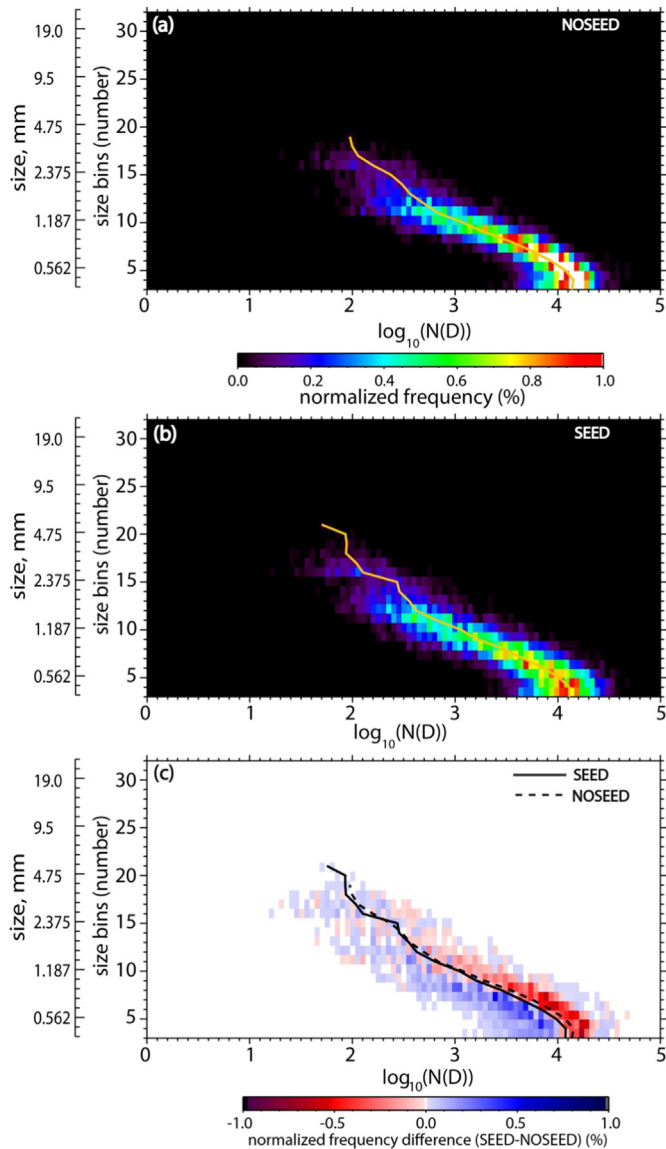
$$ZIP = \Delta dBZ_T - \Delta dBZ_U \qquad (2)$$

Fig. 16. Frequency by diameter display (FDD) of snow particle concentration measured by the Parsivel at Battle Pass during the (a) NOSEED and (b) SEED periods. Panel (c) shows the normalized frequency difference FDD between SEED and NOSEED. The solid yellow lines in (a) and (b) show the average value; these lines are repeated as black lines in (c). (For interpretation of the references to colour in this figure legend, the reader is referred to the web version of this article.)

In other words, ZIP (Z impact parameter) is the difference between the average reflectivity change [SEED – NOSEED] in the target region (or treated, subscript T) and that in the control region (untreated, subscript U). Here $\Delta dBZ = dBZ_S - dBZ_N$, with subscript S (N) refering to SEED (NOSEED).

To qualitatively relate this change to precipitation impact, we express ZIP as a relative change in precipitation rate (R), assuming a Z ($mm^6\,m^{-3}$) – R ($mm\,h^{-1}$) relationship. Again following Pokharel et al. (2014a), the precipitation impact factor (PIF) is defined as a relative change in R (SEED vs. NOSEED) in the target area, relative to the same relative change in the untreated area:

$$PIF = \frac{\frac{R_{S,T}}{R_{N,T}}}{\frac{R_{S,U}}{R_{N,U}}} \tag{3}$$

The PIF can be related to ZIP, $PIF = 10^{\left(\frac{b \times ZIP}{10}\right)}$, if one assumes a Z-R relationship of the form $R = aZ^b$, where a and b are constants (Pokharel et al., 2014a). While a range of empirically determined values of b can be found in the literature, not just for cm-wave radars but also mm-wave radars (Pokharel and Vali, 2011; Matrosov, 2007), we use a single value ($b = 0.7$) for the three radars, for simplicity, since quantitative precipitation impact estimation is beyond the scope of this case study.

The profiles of ZIP and corresponding PIF for three radars are shown in Fig. 14. For all three radar systems, the control area is *upwind* of the target area. All three radars show positive ZIP values (PIF > 1) within the well-mixed boundary layer, which is estimated to be 600 m deep on average, based on WCR vertical velocity spectra. If we consider the change in the control area as the natural regional trend, and change in target region as this natural trend plus the seeding impact, then we conclude that all three radars agree that seeding increases reflectivity (and thus precipitation rate). Since precipitation was measured by ETI gauges during the IOP both in the control region (*lateral* control, Elk River, Fig. 1) and in the target region (the average of two ETI gauges, one at Battle Pass and one a few km further downwind), we can calculate the PIF based on measured surface precipitation using Eq. (3). This gauge-based PIF also is larger than one (Fig. 14). While the different radar systems and gauge network, each with their own control and target regions, their own measurement properties, and their own slightly different observational periods (Table 2), all agree on the sign of the change, they differ on the magnitude of that change.

5. Seeding impact detection: in situ particle measurements on the ground

To better understand the observed increase in low-level reflectivity at Battle Town site (Fig. 1) during SEED, as observed by the MRR (Fig. 9) and the DOW (Fig. 12c), we examine data from the particle sizing and imaging probes at that site. As discussed in Section 4.2, there is good evidence that this site was impacted by AgI seeding, although with some delay. A Parsivel disdrometer measures particle concentration in 32 size bins ranging from 0.062 to 24.5 mm in diameter. No clear trend was observed in the particle concentration in the various size bins during the IOP (Fig. 15a). In general ice particles remained small throughout the storm, but the particle concentration tended to peak in the middle of the IOP, with lower values both early and late in the IOP (Fig. 15b). The Parsivel measured particle size distribution can be used to calculate equivalent reflectivity assuming Rayleigh scattering: the calculated reflectivity trend (Fig. 15c) matches the mean particle size trend (Fig. 15b). On average Parsivel-estimated reflectivity is higher during SEED (48.7 dBZ) compared to NOSEED (45.9 dBZ); at least in sign, this change is consistent with the MRR and DOW data at Battle Town site.

These Parsivel data are composited as frequency-by-diameter displays (FDDs) to detect changes in particle size distributions (PSDs) between the two periods (Fig. 16). Two features are apparent; first, on average the PSD tends to drop off exponentially with size, as expected, and second, the distribution of PSDs is very narrow during both periods (Fig. 16a and b). The *difference* FDD shows a higher concentration of small snow particles during NOSEED (Fig. 16c), while the concentration of the largest particles (> 2 mm) (which dominate the calculated reflectivity) is slightly higher during SEED. This result is inconsistent with the expectation that the observed increase in reflectivity during glaciogenic seeding is due at least in part to an increase in particle concentration. In any event, the differences are rather small, and, as evident from Fig. 15, sensitive to the choice of time periods.

Aside from the Parsivel, there also was a CPI probe on the scaffold at Battle Town site, imaging ice particles in fine detail (~10 μm resolution) as they floated through an aspirated tube. Select CPI particle images during this IOP are shown in Fig. 17. A variety of mostly
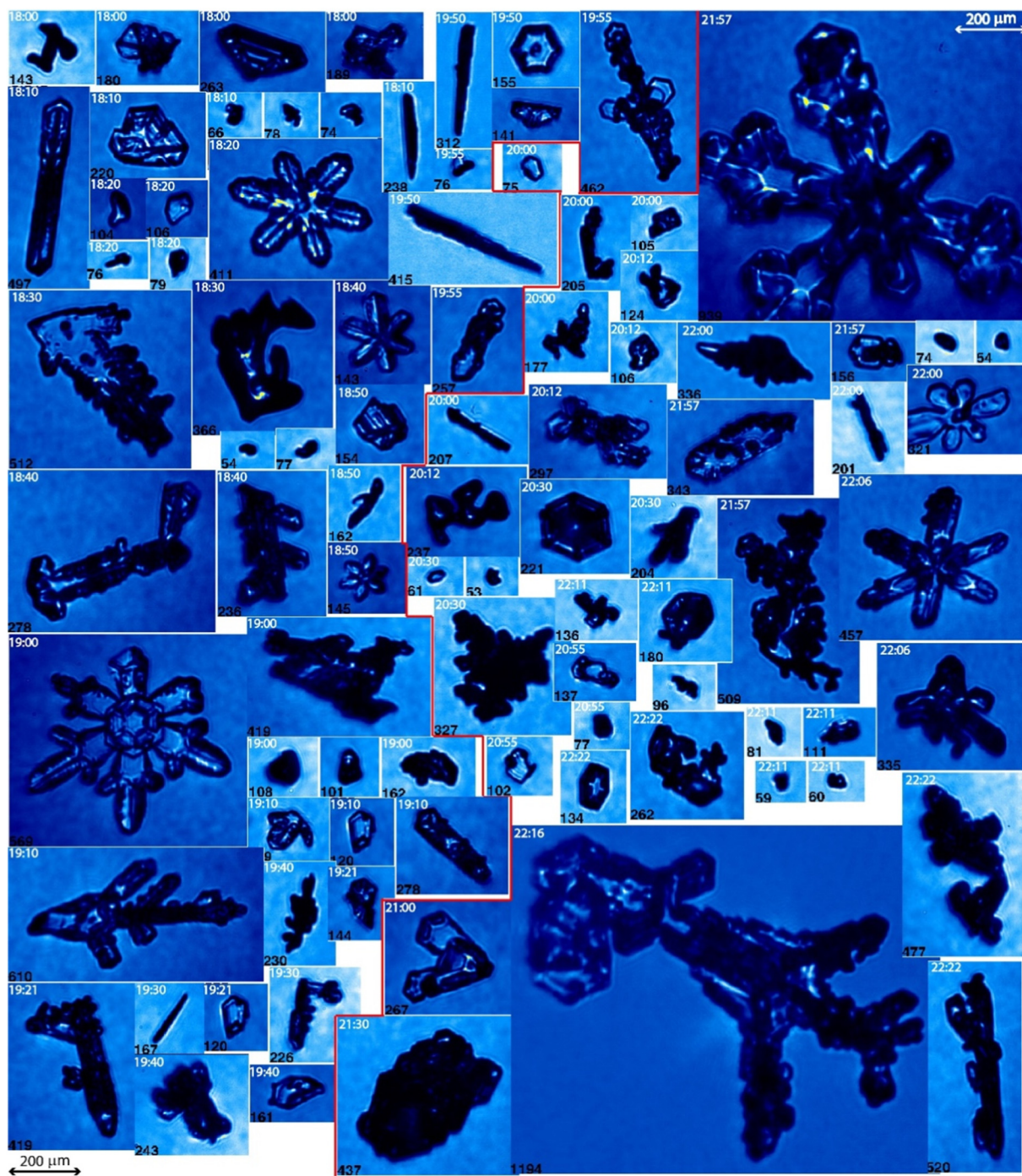
Fig. 17. A sampling of snow crystal images measured by the Cloud Particle Imager (CPI) at Battle Town site (Fig. 1) during the IOP. The scale is shown at the top right and bottom left. The time (UTC) is shown in the upper left corner of each sample. Time increases from upper left to lower right. The red line separates NOSEED (left) from SEED (right) periods. The black number in lower left corner of individual images shows the maximum particle dimension, in microns. (For interpretation of the references to colour in this figure legend, the reader is referred to the web version of this article.)

unrimed crystal habits were observed, including columns, needles, plates, dendrites, as well as aggregates. A qualitative analysis of the collage from the upper left (near 1800 UTC) to the lower right (near 2222 UTC) reveals many larger crystals or aggregates during SEED.

6. Conclusions

A case study of the impact of glaciogenic seeding on a shallow, naturally precipitating, stratiform orographic cloud observed on 3 March 2012 (IOP17) during the ASCII field experiment over the Sierra Madre range in southern Wyoming is presented. This persistent cloud was documented by three different radar systems and several airborne and ground-based particle sizing and imaging probes. The cloud base temperature was $\sim -9\,°C$ and cloud top temperature $\sim -16\,°C$, which is a suitable temperature range for AgI seeding. The flow was unblocked and the surface winds were strong over the mountain (~ 15–$20\,\mathrm{m\,s^{-1}}$), implying a high probability that ground-released AgI nuclei were mixed effectively into cloud, whose base was below mountain crest level. Natural ice crystal concentrations in this orographic cloud were small, as the cloud top was relatively warm, the seeder-feeder mechanism

(crystals falling from an ice cloud aloft) was not active (according to WCR reflectivity profiles), and conditions were not suitable for ice multiplication. Growth occurred by vapor diffusion (the Bergeron process), as droplets were quite small and airborne and ground-based particle imaging probes revealed little or no riming.

The impact of seeding on snow particle properties is not immediately obvious from instantaneous reflectivity or maps, thus the impact of AgI seeding is studied by contrasting the measurements collected before seeding commenced (NOSEED) against those during seeding (SEED), both in a target region and in an upwind control region. The airborne probes have shorter SEED and NOSEED periods compared to the ground-based ones, but the key findings listed below apply irrespective of the definition of SEED and NOSEED periods. A higher-than-expected Ag concentration was found in a fresh snow sample collected at Battle Town site in the target region during SEED, indicating that AgI plumes (or AgI-impacted snow) probably reached that site, although only two hours after the AgI generators were switched on.

Two key conclusions are drawn:

- Three different radar systems, each with a different observational strategy, frequency, and control vs. target regions, indicate an increase in low-level reflectivity in the target region, after the natural trend in the control region is removed. This change is consistent with two other published ASCII case studies of the impact of ground-based AgI seeding on stratiform orographic clouds (IOP12 and IOP13). This finding suggests that AgI seeding increased the surface precipitation rate in IOP17, as confirmed by gauge-based snowfall measurements.

- The increase in reflectivity in this case does not appear to be due to an increase in overall ice particle concentration, but rather to more numerous large particles (aggregates) during SEED, as suggested by a Parsivel disdrometer and a Cloud Particle Imager located in the target area. This is confirmed by observed low-level X-band ZDR values, which were significantly larger for any reflectivity value in the target area during SEED, indicating that a particle of a given size was more likely to be an aggregate (higher ZDR) during SEED. This finding is not consistent with the two other stratiform cloud case studies (IOP12 and IOP13), nor with several convective cloud case studies (summarized in Pokharel et al., 2017). In all those studies, an increase in *concentration* of snow particles of all sizes was observed during SEED. In those studies, the natural ice particle concentration was higher than in IOP17. This finding is attributed to the abundance of supercooled droplets in IOP17, and the relatively low natural ice crystal concentration.

Confidence in the findings presented here mainly follows from the consistency between independent measurements. To validate these findings, we recommend a cloud-resolving numerical simulation of this case, with an AgI cloud seeding parameterization such as that by Xue et al. (2013).

Acknowledgements

References

Breed, D., Rasmussen, R., Weeks, C., Boe, B., Deshler, T., 2014. Evaluating winter orographic cloud seeding: design of the Wyoming Weather Modification Pilot Project. J. Appl. Meteor. Climatol. 53, 282–299.

Chu, X., Geerts, B., Xue, L., Rasmussen, R., 2014. Radar observations and WRF LES simulations of the impact of ground-based glaciogenic seeding effect on orographic clouds and precipitation: part i: observations and model validations. J. Appl. Meteor. Climat. 53, 2264–2286.

Chu, X., Geerts, B., Xue, L., Rasmussen, R., 2017a. Large Eddy Simulations of the impact of ground-based glaciogenic seeding on shallow orographic convection: a case study. J. Appl. Meteor. Climat. 56, 69–84.

Chu, X., Geerts, B., Xue, L., Pokharel, B., 2017b. A case study of cloud radar observations and large-eddy simulations of a shallow stratiform orographic cloud, and the impact of glaciogenic seeding. J. Appl. Meteor. Climatol. 56, 1285–1304.

Demott, P.J., 1999. Report to Ice Crystal Engineering on Tests of Ice Nucleating Ability of Aerosols Produced by New Formulation Pyrotechnics – July 1999, Report. Cloud Simulation and Aerosol Laboratory, Department of Atmospheric Science, Colorado State University, Fort Collins, CO (30 pp.).

French, J.R., Friedrich, K., Tessendorf, S., Rauber, R., Geerts, B., Rasmussen, R., Xue, L., Kunkel, M., Blestrud, D., 2018. Precipitation formation from orographic cloud seeding. Proc. Natl. Acad. Sci. U. S. A. https://doi.org/10.1073/pnas.1716995115.

Garstang, M., Bruintjes, R., Serafin, R., Orville, H., Boe, B., Cotton, W., Warburton, J., 2005. Finding common ground. Bull. Am. Meteor. Soc. 86, 647–655.

Geerts, B., Miao, Q., Yang, Y., Rasmussen, R., Breed, D., 2010. An airborne profiling radar study of the impact of glaciogenic cloud seeding on snowfall from winter orographic clouds. J. Atmos. Sci. 67, 3286–3302.

Geerts, B., Pokharel, B., Friedrich, K., Breed, D., Rasmussen, R., Yang, Y., Miao, Q., Haimov, S., Boe, B., Kalina, E., 2013. The AgI seeding cloud impact investigation (ASCII) campaign 2012: overview and preliminary results. J. Weather Mod. 45, 24–43.

Geerts, B., Pokharel, B., Kristovich, D.A.R., 2015. Blowing snow as a natural glaciogenic cloud seeding mechanism. Mon. Wea. Rev. 143, 5017–5033.

Houze Jr., R., 2014. *Cloud Dynamics.* International Geophysics Series Vol. 104, 2nd edition. (496 pp.).

Jing, X., Geerts, B., 2015. Dual-polarization radar data analysis of the impact of ground-based glaciogenic seeding on orographic clouds. Part II: convective clouds. J. Appl. Meteor. Climatol. 54, 2099–2117.

Jing, X., Geerts, B., Friedrich, K., Pokharel, B., 2015. Dual-polarization radar data analysis of the impact of ground-based glaciogenic seeding on winter orographic clouds. Part I: mostly stratiform clouds. J. Appl. Meteor. Climatol. 54, 1944–1969.

Jing, X., Geerts, B., Boe, B., 2016. The extra-area effect of orographic cloud seeding: observational evidence of precipitation enhancement downwind of the target mountain. J. Appl. Meteor. Climatol. 55, 1409–1424.

Kumjian, M.R., 2013. Principles and applications of dual-polarization radar. Part II: warm and cold season applications. J. Operational Meteor. 1 (20), 243–264.

Lawson, R.P., Baker, B.A., Zmarzly, P., O'Connor, D., Mo, Q., Gayet, J.F., Shcherbakov, V., 2006. Microphysical and optical properties of atmospheric ice crystals at South Pole Station. J. Appl. Meteor. Climatol. 45, 1505–1524.

Löffler-Mang, M., Joss, J., 2000. An optical disdrometer for measuring size and velocity of hydrometeors. J. Atmos. Ocean. Technol. 17, 130–139.

Maahn, M., Kollias, P., 2012. Improved Micro Rain Radar snow measurements using Doppler spectra post-processing. Atmos. Meas. Tech. 5, 2661–2673.

Matrosov, S.Y., 2007. Modeling backscatter properties of snowfall at millimeter wavelengths. J. Atmos. Sci. 64, 1727–1736.

Matrosov, S.Y., Campbell, C., Kingsmill, D., Sukovich, E., 2009. Assessing snowfall rates from X-band radar reflectivity measurements. J. Atmos. Ocean. Technol. 26, 2324–2339.

National Research Council, 2003. Critical Issues in Weather Modification Research. National Academies Press (42 pp.).

Pokharel, B., Geerts, B., 2016. A multi-sensor study of the impact of ground-based glaciogenic seeding on clouds and precipitation over mountains in Wyoming. Part I: Project description. Atmos. Res. 182, 269–281.

Pokharel, B., Vali, G., 2011. Evaluation of collocated measurements of radar reflectivity and particle sizes in ice clouds. J. Appl. Meteor. Climatol. 50, 2104–2119.

Pokharel, B., Geerts, B., Jing, X., 2014a. The impact of ground-based glaciogenic seeding on orographic clouds and precipitation: a multi-sensor case study. J. Appl. Meteor. Climatol. 53, 890–909.

Pokharel, B., Geerts, B., Jing, X., Friedrich, K., Aikins, J., Breed, D., Rasmussen, R., Huggins, A., 2014b. The impact of ground-based glaciogenic seeding on orographic clouds and precipitation: a multi-sensor case study. Atmos. Res. 147-148, 162–181.

Pokharel, B., Geerts, B., Jing, X., 2015. The impact of ground-based glaciogenic seeding on clouds and precipitation over mountains: a case study of shallow orographic cloud with large supercooled droplets. J. Geophys. Res. 120, 6056–6079.

Pokharel, B., Geerts, B., Jing, X., Friedrich, K., Ikeda, K., Rasmussen, R., 2017. A multi-sensor study of the impact of ground-based glaciogenic seeding on clouds and precipitation over mountains in Wyoming. Part II: seeding impact analysis. Atmos. Res. 183, 42–57. https://doi.org/10.1016/j.atmosres.2016.08.018.

Politovich, M.K., Vali, G., 1983. Observations of liquid water in orographic clouds over Elk Mountain. J. Atmos. Sci. 40, 1300–1312.

Rasmussen, R., Dixon, M., Vasiloff, S., Hage, F., Knight, S., Vivekanandan, J., Xu, M., 2003. Snow nowcasting using a real-time correlation of radar reflectivity with snow gauge accumulation. J. Appl. Meteorol. 42, 20–36.

Rotunno, R., Houze, R.A., 2007. Lessons on orographic precipitation from the Mesoscale Alpine Programme. Q. J. R. Meteor. Soc. 133, 811–830.

Tessendorf, S., et al., 2018. Transformational approach to winter orographic weather modification research: the SNOWIE Project. Bull. Amer. Meteor. Soc (in review).

Wang, Z., French, J., Vali, G., Wechsler, P., Haimov, S., Rodi, A., Deng, M., Leon, D., Snider, J., Peng, L., Pazmany, A.L., 2012. Single aircraft integration of remote sensing and in situ sampling for the study of cloud microphysics and dynamics. Bull. Am. Meteor. Soc. 93, 653–668.

Wolfe, J.P., Snider, J.R., 2012. A relationship between reflectivity and snow rate for a high-altitude S-band radar. J. Appl. Meteor. Climatol. 51, 1111–1128.

Wurman, J., Straka, J., Rasmussen, E., Randall, M., Zahrai, A., 1997. Design and deployment of a portable, pencil-beam, pulsed, 3-cm Doppler radar. J. Atmos. Ocean. Technol. 14, 1502–1512.

Xue, L., Hashlmoto, A., Murakami, M., Rasmussen, R., Tessendorf, S., Breed, D., Parkinson, S., Holbrook, P., Blestrud, D., 2013. AgI cloud seeding effects as seen in WRF simulations. Part I: model description and idealized 2D sensitivity tests. J. Appl. Meteor. Climatol. 52, 1433–1457.

Xue, L., Chu, X., Rasmussen, R., Breed, D., Geerts, B., 2016. A case study of radar observations and WRF LES simulations of the impact of ground-based glaciogenic seeding on orographic clouds and precipitation. Part II: AgI dispersion and seeding signals simulated by WRF. J. Appl. Meteor. Climatol. 55, 445–464.

Yuter, S., Houze, R.A., 1995. Three-dimensional kinematic and microphysical evolution of Florida cumulonimbus. Part II: frequency distributions of vertical velocity, reflectivity, and differential reflectivity. Mon. Wea. Rev. 123, 1941–1963.

Yuter, S.E., Kingsmill, D.E., Nance, L.B., Löffler-Mang, M., 2006. Observations of precipitation size and fall speed characteristics within coexisting rain and wet snow. J. Appl. Meteor. Climatol. 45, 1450–1464.